

COOLING CURVES OF CONCENTRATED ALLOYS, STEELMAKING SLAG, AND LITHIUM IRON PHOSPHATE

Delin Li 

CanmetMATERIALS, Natural Resources Canada, 183 Longwood Road South, Hamilton, ON L8P 0A5, Canada

Copyright © 2024 Crown
<https://doi.org/10.1007/s40962-024-01323-7>

Abstract

Over the past few years, a variety of melting casting projects have been performed, in collaboration with industries and universities. Concentrated alloys and nonmetallic compounds were studied including high-Si cast iron, high-Mn steel, Al-added stainless steel, high-entropy alloy, Permalloy 80 Ni alloy, Stellite Co alloy, steelmaking slag, and lithium iron phosphate (LFP). A melt synthesis of LFP was developed. Cooling curves were measured using the thermal analysis cup method and differential thermal analysis. In addition, the phase diagrams of alloys were

calculated using Thermo-Calc. This paper draws on some examples of the measured cooling curves to illustrate the thermal behaviors of melts, along with a quick review of each project.

Keywords: cooling curves, high-Si iron, high-Mn steel, Al-added stainless steel, high-entropy alloy, permalloy, stellite alloy, steelmaking slag, lithium iron phosphate, LFP

Introduction

Thermal analysis (TA) and cooling curves (CC) can be used in many ways and are often used to determine the liquidus and solidus temperatures which are helpful to improve the metalcasting process.¹ There have been immense research and applications of TA for cast iron,² low alloy steel,³ and aluminum alloys.⁴ However, few reports are available about the cooling curves of concentrated alloys and nonmetallic materials.

In recent years, various experimental studies have been performed in CanmetMATERIALS, including high-Si cast iron, high-Mn steel, Al-alloyed stainless steel, high-entropy alloy (HEA), Permalloy 80 Ni alloy, Stellite Co alloy, steelmaking slag, and lithium iron phosphate (LFP). Cooling curves were measured using the TA cup method during the melting casting experiments. LiFePO_4 is a promising cathode material for lithium-ion battery. It is commercially produced mainly using two methods: solid-state and hydrothermal processes. A novel melt synthesis of LFP has been developed to reduce cost.^{5,6} This paper

presents the measured cooling curves and calculated phase diagrams, together with a brief introduction of each project.

Experimental Procedures

An induction furnace of 100 kW was utilized with a crucible of 200 mm (8 in.) diameter and 50 kg (110 lb) steel capacity. The SPAL (Surface Protection Air Liquid) lance was installed on the furnace, as shown in Figure 1. The liquid argon stream from SPAL was applied prior to incipient melting and was maintained throughout the melting casting cycle. Keel blocks, ingots, and shaped parts were cast in the experiments. In addition, the Thermal Analysis (TA) cup samples were poured, as shown in Figure 2. Two types of TA cups were utilized: S-type and K-type thermocouples. The dimensions of TA cup are approximately 38 mm (1.5 in.) diameter, side length, and depth. DTA (Differential thermal analysis) testing was conducted on some of cast samples. The DTA standard procedures were described in a website.⁷ Eight groups of materials studied in this work are summarized in Table 1. The main objective of the projects was to continuously improve the existing alloy formulas and manufacturing process.

This paper is based upon one in the AFS Transactions Vol. 132.

Received: 29 February 2024 / Accepted: 01 March 2024

Published online: 28 April 2024

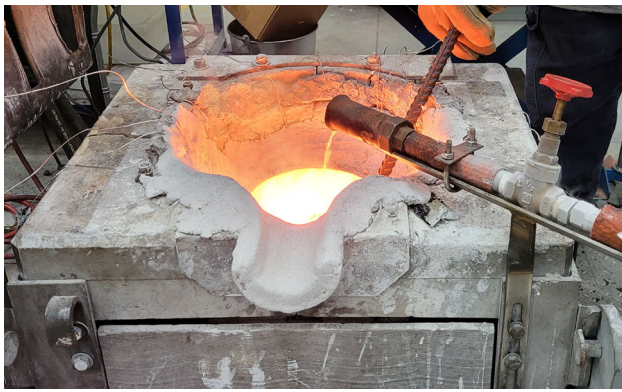


Figure 1. Melting experiments using 100-kW induction furnace with SPAL installed.

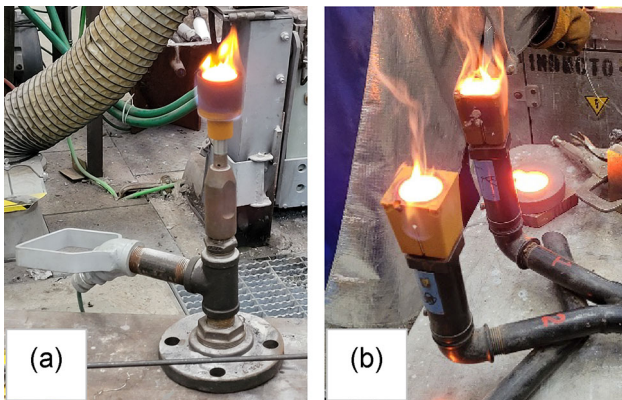


Figure 2. Measurements of cooling curves using the TA cup method: (a) S-type and (b) K-type thermocouples.

Results and Discussion

High-Silicon Cast Iron

Recently, a critical minerals strategy was announced.¹⁵ It was reported that sulfuric acid roasting was a major process for decomposition of rare earth concentrate, which is commercially practiced in a rotary kiln (RK).¹⁶ The liner wall of RK is susceptible for elevated-temperature acid corrosion, thus a very short life. Hi-Si iron could be one of the candidates for the liner material of RK. It is a special iron for corrosion resistant applications, which contains up to 14–18% Si (composition in wt% was used throughout this paper) in ASM handbook¹⁷ and ASTM standards A518 and A861. At this stage, we cast Keel-block samples of 24 × 170 mm (1 × 7 in.) using no-bake sand molds for material and process evaluations. The alloys were poured at ~1345 °C (2455 °F). In-mold inoculant of 0.07% FeSi (Elkem) was added. Two compositions of samples were cast per ASTM A518: melt 1A (Grade 1, 14.5% Si) and melt 1B (melt 1A plus 5% Cu and 0.05% rare earth mainly Ce). The chemical compositions were analyzed using OES (Optical emission spectrometry), XRF (X-ray fluorescence), and ICP-AES (Inductively coupled plasma atomic emission spectroscopy). Additions of copper and rare earth

Table 1. Eight Groups of Materials Studied in This Work

Mater. ID	Material type, formula, and composition (wt%)	References
Hi-Si	High-Si Cast Iron in ASTM A518 and Modified: 14.5Si, 0.9C, 0.5Mn, 0 and 5.0Cu.	8
Hi-Mn	High-Mn Steel in ASTM A128: 18.0Mn, 2.0Cr, 1.2C, 0.5Si.	9
Al-St	Al-added Stainless Steel: 0 to 5.5Al, 25Ni, 20Cr, 0.9Si, 0.9Mn, 0.1C.	10
Ni _{2.1}	Eutectic HEA, AlCoCrFeNi _{2.1} : 8.5Al, 18.6Co, 16.4Cr, 17.6Fe, 38.9Ni.	11
Ni80	ASTM A753, Type 4 Permalloy 80: e.g., 80Ni, 15Fe, 5Mo.	12
SF12	Cobalt-base Alloy, Stellite: 19Cr, 14Ni, 9W, 3Si, 2Fe, 2B, 0.9C.	13
Slag	EAF Steelmaking Slag: e.g., 38CaO, 25FeO, 14SiO ₂ , 10MgO, 6Al ₂ O ₃ , 6MnO.	14
LFP	A Cathode Material for Lithium-ion Battery, Lithium Iron Phosphate, LiFePO ₄ .	5, 6

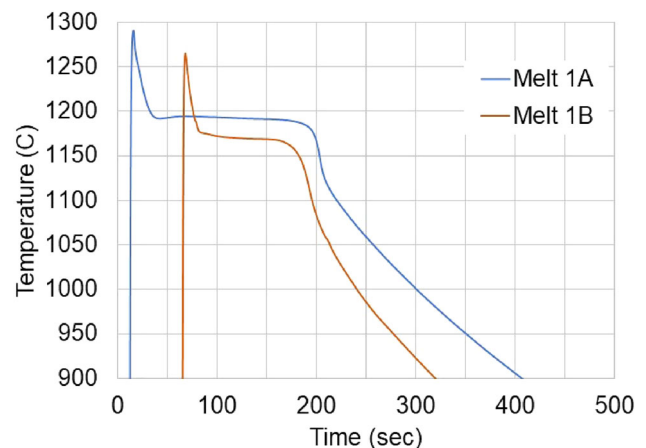


Figure 3. Measured cooling curves of 14.5% Si iron: melt 1A (Grade 1 of ASTM A518) and melt 1B (melt 1A plus 5% Cu and 0.05% Ce).

were reported to improve the mechanical and corrosion properties of Hi-Si cast iron.¹⁸ In addition, rare earth played a role in deoxidation of the low-carbon high-silicon iron melts. The thermal arrests in Figures 3 and 4 can be found to estimate the liquidus T_L and solidus T_S temperatures, because of low undercooling and cooling rate that usually occur in the TA cup samples. The T_L and T_S (eutectic plateau T_E) of melt 1A were determined as 1190 °C (2175 °F) and 1180 °C (2155 °F), respectively, from the cooling curves, which agrees with the calculated phase

diagram in Figure 5a. A comparison of the calculated phase diagrams Figure 5a and b shows that the additions of 5% Cu and 0.05% Ce (melt 1B) reduced the eutectic carbon content by 0.1% C and increased the eutectic temperature T_E by 10 °C. In contrast to the calculations, the measured T_E of melt 1B was decreased by 15 °C compared to melt 1A, as shown in Figure 3. This could be due to the Ce-induced undercooling which is not reflected in the equilibrium phase diagrams. Cerium is known as a promotor of chunk graphite microstructure in cast iron as shown Figure 6b.

Type A graphite flakes are randomly distributed and oriented throughout the samples of melt 1A, as shown in Figure 6a. The flake graphite was transformed to chunky graphite (Figure 6b) due to the addition of Ce. The Cu-rich phase was formed in melt 1B (Figure 6b). The 14.5% Si iron is much more susceptible to gas porosity defects than other iron castings of lower Si, e.g., 4.5% Si iron. A set of corrosion testing was completed on the Hi-Si cast iron samples as compared to wrought stainless steel 304. The samples were machined using EDM (electrical discharge machining). The sample dimensions were 20 mm diameter and 4 mm thick. The immersion testing was conducted in 98% sulfuric acid for 30 days, at room temperature of 60

°C (140 °F), respectively. Besides, the electrochemical corrosion testing was completed. As confirmed, this grade of Hi-Si cast iron showed superior corrosion resistance and improvements over the stainless steel 304.

High Manganese Steel

High-Mn steel castings, or Hadfield steel, with 12–22% Mn, 1.0–1.5% C are widely used as critical components in cement, mining, and construction operations due to their excellent wear resistance, work hardenability, and formability.⁹ Although 10 grades of austenitic Mn steel are identified in ASTM standard A128, continuous research work has been carried out, e.g., adding alloying elements Al, Cr, Mo, Ti, and V.¹⁹ Some producers had their success in implementing the various grain refinement techniques, but the most reliable method to obtain a fine grain structure is to pour the metal with low superheat.¹⁹ The recommended pouring temperature was 1400 °C (2550 °F). The TA cup samples were poured to obtain the cooling curves of Hi-Mn steel samples (Figure 7). Because of low pouring temperatures, the superheated stage of liquid steel was missed out for the cooling curves except curve #5 in Figure 7. The T_L of the 18% Mn steel samples was determined as 1360 °C (2480 °F) from the cooling curves. This is close to the calculated T_L from the phase diagram at 1.2% C (Figure 8). Heat treatment to a temperature at least 1000 °C (1830 °F), and quenching in water, was conducted to achieve toughness and ductility per ASTM standard A128.

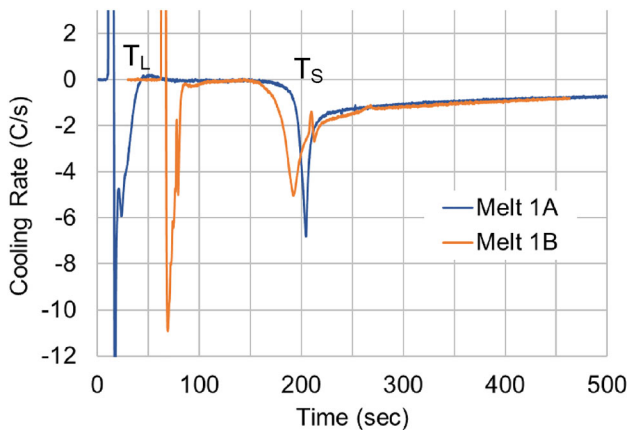


Figure 4. Cooling rates of melt 1A and melt 1B.

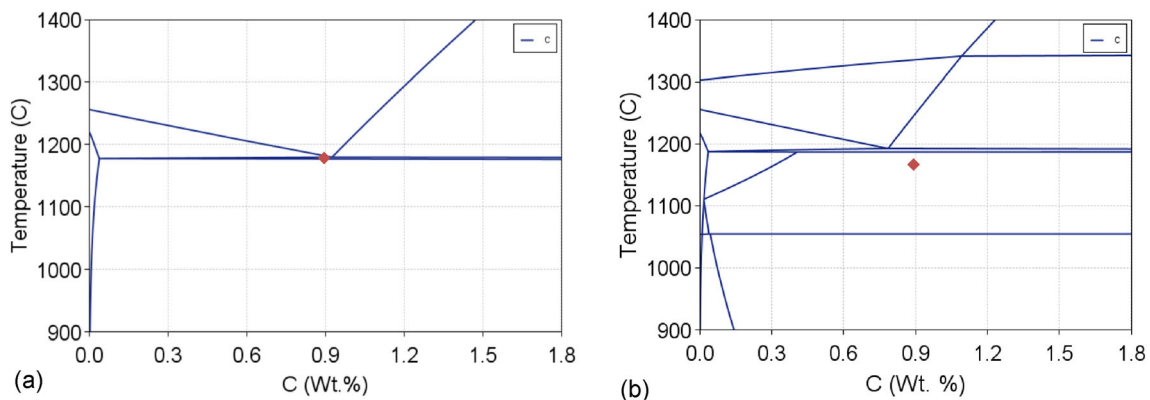


Figure 5. Calculated phase diagrams of Hi-Si (14.5% Si) iron with measurements of cooling curves (dots): (a) melt 1A and (b) melt 1B.

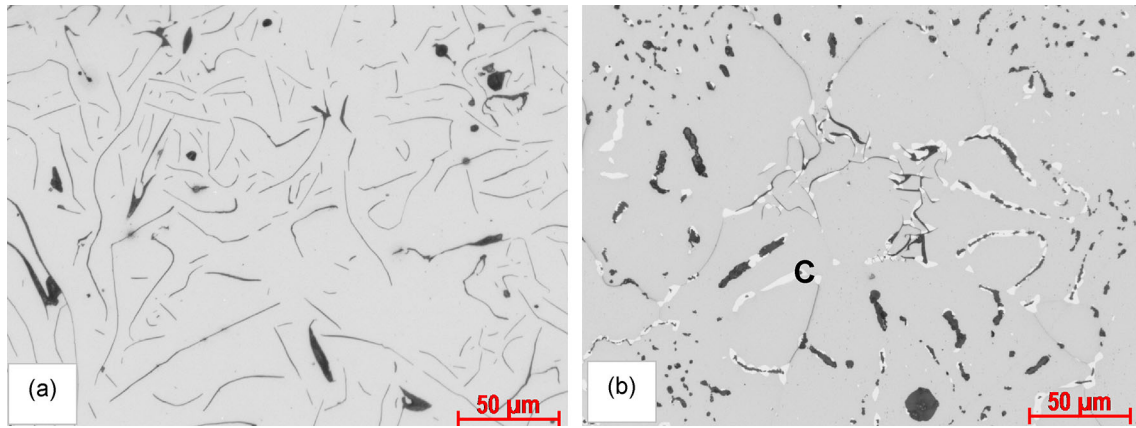


Figure 6. Micrographs of 14.5% Si iron samples: (a) flake graphite from melt 1A and (b) chunk graphite and Cu-rich phase (bright phase marked as "C") from melt 1B.

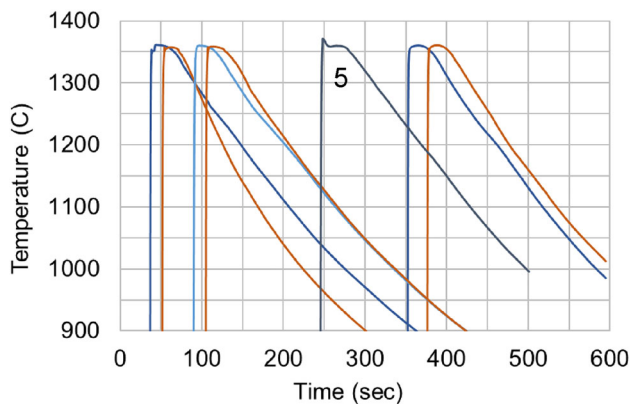


Figure 7. Measured cooling curves of Hi-Mn steel from 7 TA cup samples.

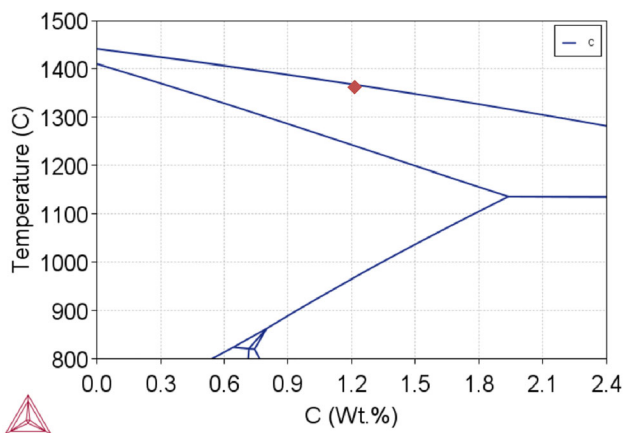


Figure 8. Calculated phase diagram of Hi-Mn steel with measurements of cooling curves (dot).

experiments as shown in Figure 9. Al-alloyed steels and irons have long been recognized as very attractive materials due to heat resistance and lightweight high strength. In this work, stainless-steel castings (20Cr- 25Ni) were made with the Al contents ranging from 0 to 5.5%. The liquidus temperature T_L was decreased by increasing the Al content

up to 4.5% Al, as shown in Figures 10 and 11. There was a good agreement between the measured liquidus and the calculated phase diagram. The 4.0% Al and 5.5% Al steel samples almost had the same liquidus temperature, 1370 °C (2500 °F), but different solidification modes. When the Al content is below 4.5%, it is austenitic stainless steel. When the Al content exceeds 4.5%, a transition of primary solidification occurred from FCC (face centered cubic) austenite to BCC (body centered cubic) as shown in Figure 11, which was also confirmed by the following microstructures (Figure 12).

Oxidation testing at 1000 °C (1830 °F) was conducted for the Al-St samples which were daily removed from a muffle furnace, weighed, and returned to the furnace. Figure 12 shows the micrographs of tested samples. Evident oxide spallation occurred during the testing for the samples of < 4% Al, as also indicated by the broken oxide scales in Figure 12a. The Al-St samples of 4.0 and 5.5% Al formed with Al_2O_3 particles adjacent to the surface as shown in Figures 12b and c, thus greatly enhancing the hot oxidation resistance. The samples of $\leq 4.0\%$ Al consist of austenitic structure. However, ferrite was solidified as a primary phase for the 5.5% Al sample (Figure 12c), which explains a huge increase in the Brinell hardness (10 mm/3000 kg), as listed in Table 2. Little or no oxide spallation was observed for the FSS (ferritic stainless steel) samples during the oxidation testing, also due to a low coefficient of thermal expansion of FSS. However, the Al content should be controlled < 4.5% for this stainless steel, if a fully austenitic structure is required for the applications. Dross formation is a noted concern for melting and casting of aluminum-alloyed steel and iron.

Eutectic High-Entropy Alloy

Unlike conventional alloys, high-entropy alloys (HEAs) have no single dominant element and use multiple principal elements. This group of alloys is also referred to as multi-

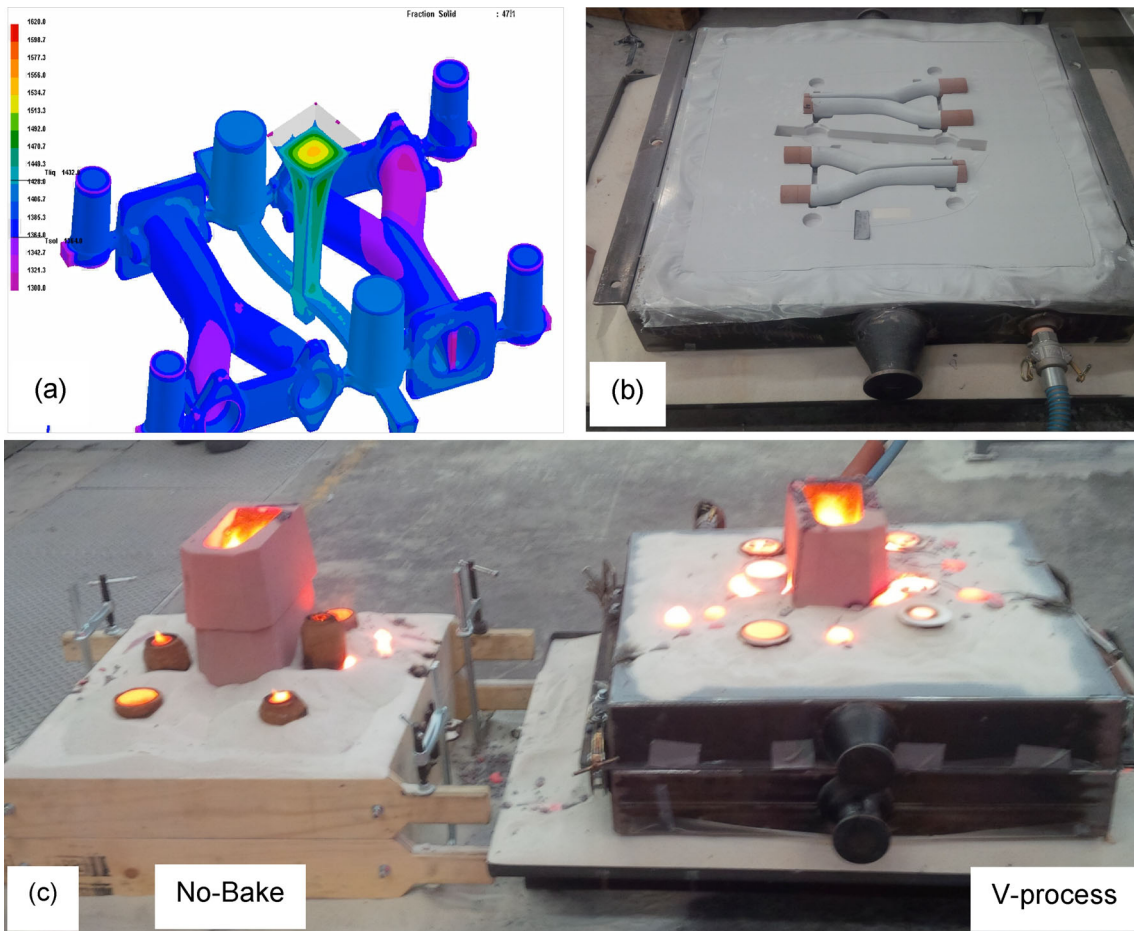


Figure 9. Casting experiments of Y-shaped manifolds using V-process: (a) simulation of flow and solidification, (b) V-process mold showing vacuum hose and plastic film adhesion, and (c) poured two molds of no-bake and V-process for comparison.

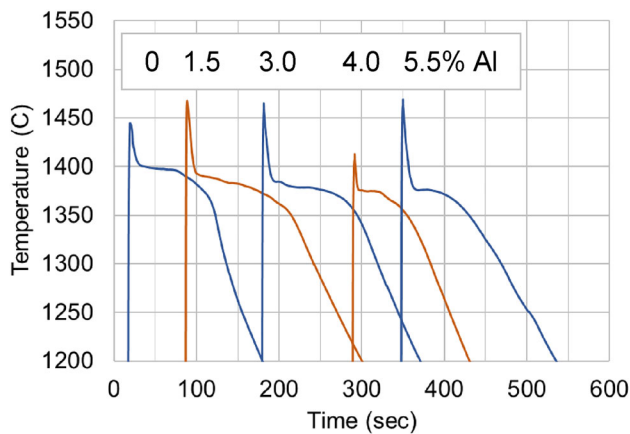


Figure 10. Measured cooling curves of Al-St samples with Al contents ranging from 0 to 5.5%.

principal element alloys (MPEA) or complex concentrated alloys (CCA).²⁰ The terms of HEA, MPEA, and CCA are used interchangeably to describe this field broadly. HEA can be classified differently, regarding alloy phase, element type and ratio, manufacturing route, alloy design method, materials property, and application, respectively, as

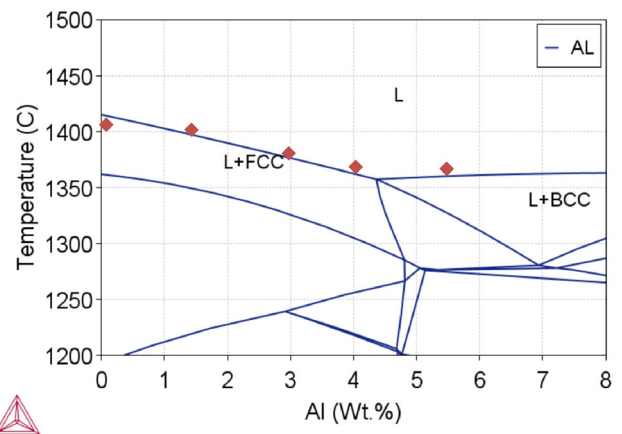


Figure 11. Calculated phase diagram of Al-St with measurements of cooling curves (dots).

summarized in Table 3. Classification is not merely about naming things but may allow one to begin taking steps toward studying of HEA. A list of abbreviations here: FCC– face centered cubic; BCC– body centered cubic; HCP– hexagonal close packed; SS– solid solution; IMC– intermetallic compound; IC– interstitial compound;

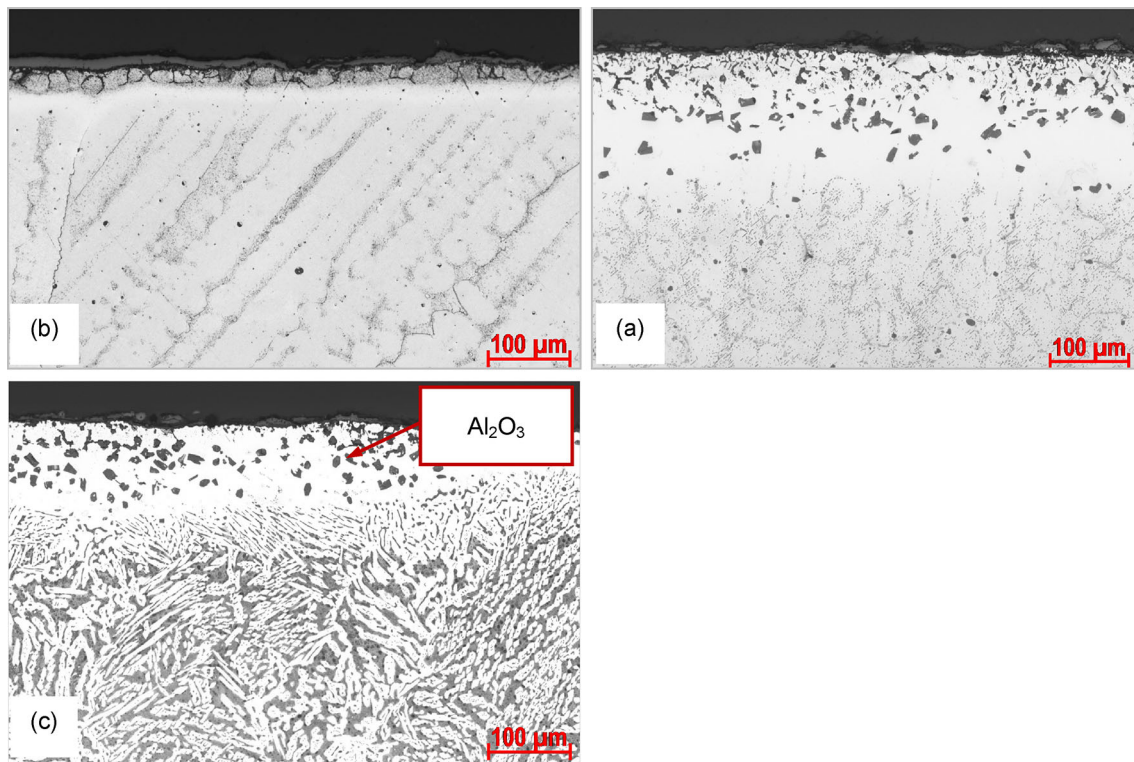


Figure 12. Micrographs of Al-St samples tested at 1000 °C (1830 °F)—400 hrs: (a) 0% Al, (b) 4.0% Al with austenitic matrix, and (c) 5.5 % Al with primary ferrite.

Table 2. Hardness and Structure of Al-St Samples

% Al	0	1.5	3.0	4.0	5.5
Hardness (HBW)	140	140	135	150	280
Primary phase	Austenite				Ferrite

MAPs– materials acceleration platforms; TWIP– twinning-induced plasticity; TRIP– transformation-induced plasticity.

Casting, forging, and rolling of HEA ingots were reported where a separate melting method was developed to produce Al-contained HEA.²¹ Measured cooling curves are shown in Figure 13. The T_L (1410 °C, 2570 °F) and eutectic temperature T_E (1335 °C, 2435 °F) determined from Figure 13 agree with the calculated phase diagram (Figure 14) at the Al content of 8.5% for the HEA $\text{AlCoCrFeNi}_{2.1}$. The microstructure of cast ingot samples consists of primary dendrite phase BCC and lamellae eutectic of BCC and FCC, as shown in Figure 15. This HEA formula appears to be a hypereutectic from the present work. In contrast, it was previously reported as a bulk eutectic composition.¹¹ The micrograph of Figure 15b at higher magnification shows ultrafine structure within the primary phase, which could be disordered BCC and ordered BCC. XRD analysis was not conducted in the present paper.

Table 3. Classifications of High-Entropy Alloys Regarding Different Criteria

Criteria	Classifications
Alloy phase	Single phase HEA: FCC, BCC, HCP, and SS. Multiphase HEA: eutectic, duplex, IMC, IC, composites, precipitates, and metastable. High-entropy metallic amorphous.
Element type	Refractory, light metal, transition metal, nonferrous HEA.
Element ratio	Equiatomic and non-equiatomic HEA.
Manufacturing route	Melting casting, mechanical alloying, additive manufacturing, powder metallurgy, vapor deposition, laser cladding, and spark plasma sintering.
Alloy design	Conventional design, MAPs, high throughput screening.
Property and application	Mechanical properties: TWIP, TRIP, wear, strength, ductility, and fracture toughness. Functional properties: anti-irradiation, magnetic, electrical, corrosion, catalytic, films, solar, thermoelectric, superconducting, cryogenic, and high temperature.

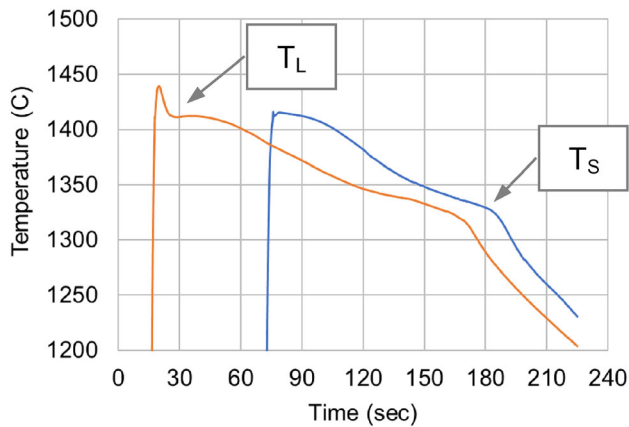


Figure 13. Measured cooling curves of eutectic HEA AlCoCrFeNi_{2.1} from 2 TA cup samples.

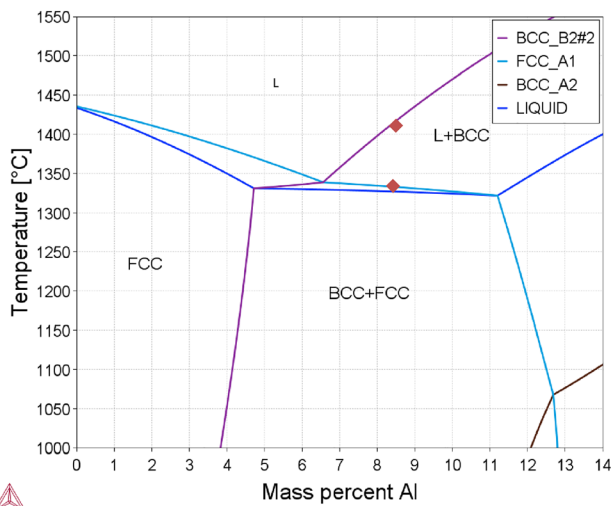


Figure 14. Phase diagram of HEA AlCoCrFeNi_{2.1} with measurements of cooling curves (dots).

Permalloy 80

Permalloy 80 (ASTM A753 Type 4) is a highly magnetic nickel-iron-molybdenum alloy, with approximately 80% Ni, 15% Fe, and 5% Mo. Permalloy 80 provides high initial and maximum permeabilities with low coercive force, hysteresis loss, eddy-current loss, and magnetostriction, which is critical for industrial applications.¹² The Canmet laboratory was requested to cast Permalloy 80 ingots. The measured cooling curves are displayed in Figure 16. Both the measured cooling curves in Figure 16 and the calculated phase diagram in Figure 17 show the liquidus temperature of 1428 °C (2600 °F). Severe gas porosity defects occurred in the Ni80 castings made from air melts even with deoxidation treatment. Finally, quality ingots of Permalloy 80 were produced using Canmet vacuum induction melting furnace.

Cobalt-Based Alloy Stellite

Stellite cobalt-based alloys consist of complex carbides in an alloy matrix. They are resistant to wear, galling, and corrosion and retain these properties at high temperatures. Their exceptional wear resistance is due mainly to the unique inherent characteristics of the hard carbide phase dispersed in a CoCr alloy matrix.¹³ The objective of this project is to study the formation of amorphous Stellite (SF12) alloy using gas atomization.²² SF12 master alloy from Kennametal (Ontario) was melted and cast into small samples in the Canmet laboratory. Then, the small samples were provided to University of Alberta for gas atomization experiments where SF12 amorphous droplets were produced.²² The T_L of 1190 °C (2175 °F) determined from the cooling curves in Figure 18 shows a good agreement with

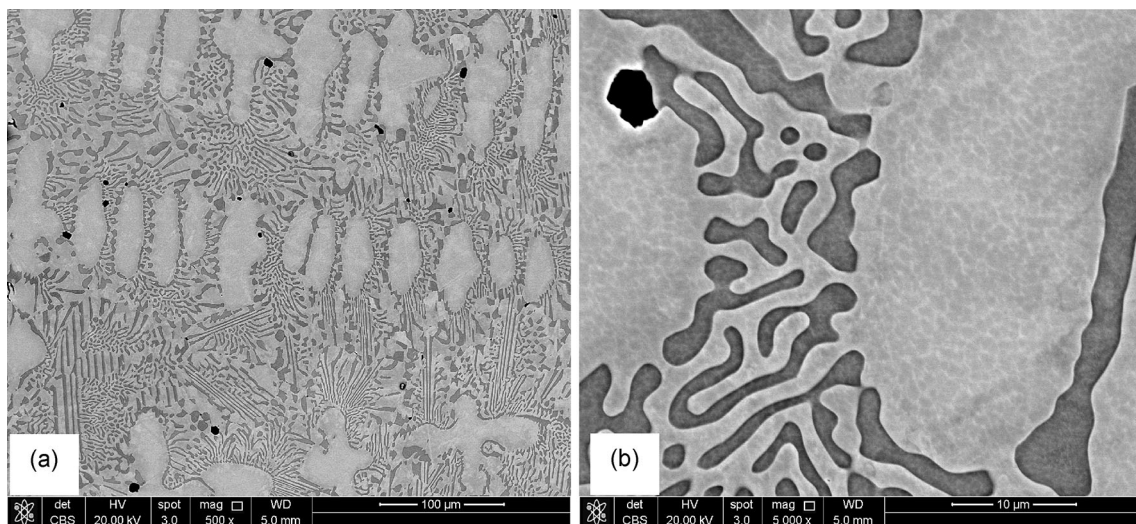


Figure 15. SEM micrographs of AlCoCrFeNi_{2.1} cast ingot sample showing: (a) primary dendrite phase and lamellae eutectic, 500× and (b) ultrafine structure within the primary phase, 5000×.

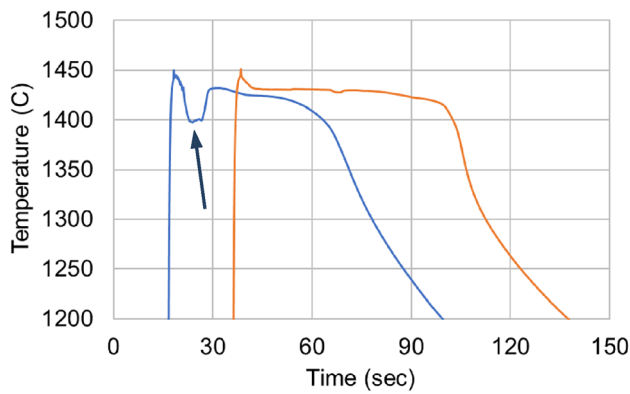


Figure 16. Measured cooling curves of Permalloy 80 from 2 TA cup samples. The curve notch pointed by an arrow is artificial.

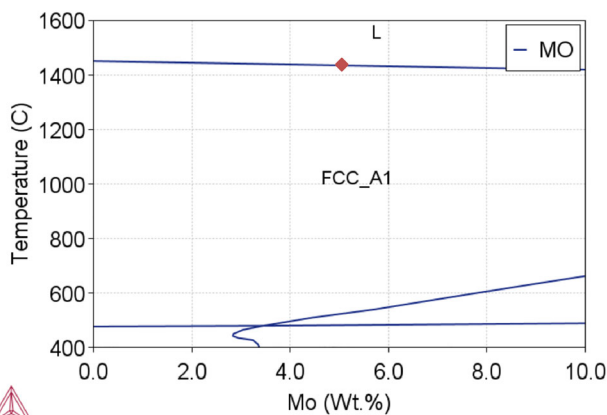


Figure 17. Calculated phase diagram of Permalloy 80 with measurements of cooling curves (dot).

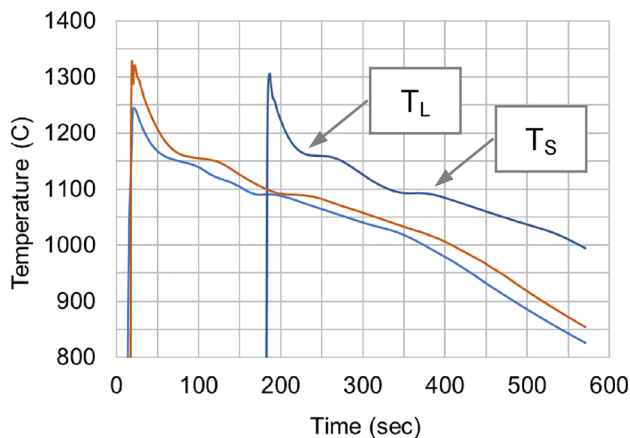


Figure 18. Measured cooling curves of Stellite SF12, Co-base alloy from 3 TA cup samples.

the phase diagram in Figure 19. The thermal arrests at 1100 °C (2010 °F) in the cooling curves (Figure 18) may correspond to the peritectic transformation shown in the phase diagram in Figure 19.

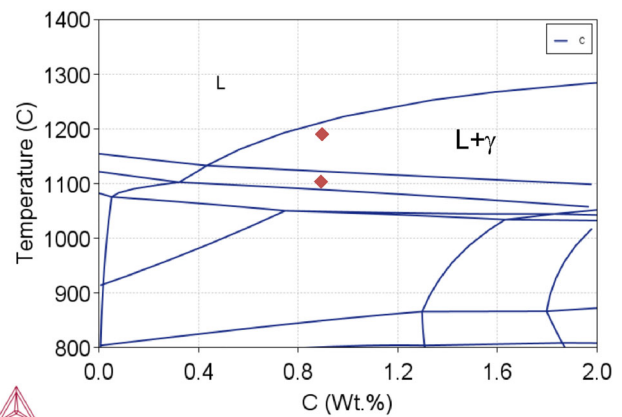


Figure 19. Calculated phase diagram of Stellite SF12, Co-base alloy with measurements of cooling curves (dots).

EAF Steelmaking Slag

Steelmaking is an energy intensive process that relies on fossil fuels to meet energy demands for primary extraction and refining of ores. The electric arc furnace (EAF) has the potential to significantly contribute to the decarbonization of the iron and steel industry. However, during some EAF steelmaking, carbon must be injected into the molten slag to generate slag foaming, which is beneficial to the energy efficiency and protection of facility.¹⁴ Most recently, our 100-kW induction melting furnace was utilized to simulate EAF steelmaking to study the slag foaming with carbon and biochar injection, as displayed in Figure 20. The slag foaming is influenced by several variables such as slag composition, viscosity, surface tension, and temperature. In this work, the TA cup method was also utilized to measure the cooling curves of molten slag, as shown in Figure 21. The T_L was estimated as 1288 °C (2350 °F) and 1400 °C (2550 °F) for slag A and B, respectively. Obviously, the T_L of slag can also be determined using DTA, e.g., 1405 °C (2560 °F) as shown in Figure 22, which is close to that of slag B tested in the TA cup (Figure 21). No phase diagram was calculated for the nonmetallic compounds, EAF slag or LFP in this work.

Lithium Iron Phosphate

The advantages of lithium iron phosphate LiFePO_4 as a cathode material include thermal stability, limited environmental impact, and potential of low cost compared to the cathode chemistries containing Co and Ni. Among many methods of synthesizing LFP, there are two processes at the industrial scale: solid state and hydrothermal. They require multiple, time-consuming steps, and costly precursors. A group of Canadian researchers has developed a novel melt synthesis of LFP to reduce cost.^{5,6} Melting cycle of induction furnace can be much shorter than that of resistance furnaces. Nonmetallic charges usually cannot be



Figure 20. Left: a cross section of crucible in induction furnace and right: image of foamy slag during melting experiment.

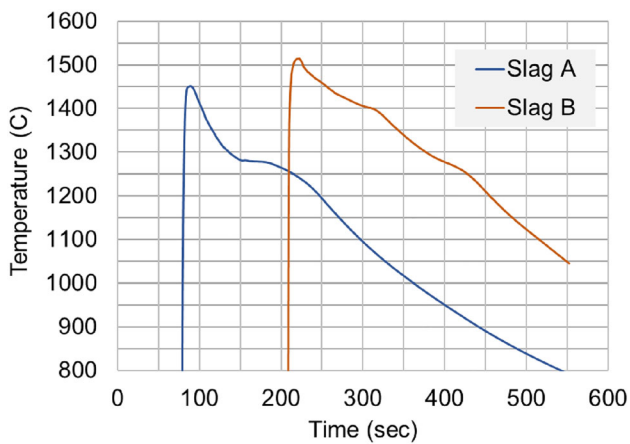


Figure 21. Measured cooling curves of EAF slag using the TA cup method.

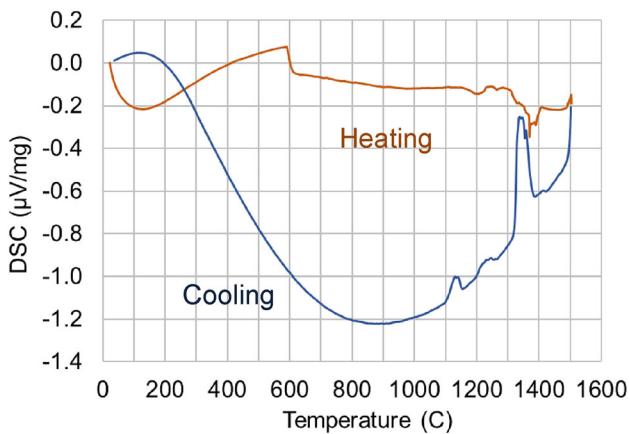


Figure 22. DTA curves of a slag sample.

directly heated by induction. In this work, a graphite crucible was utilized as susceptor to melt the inorganic precursors listed in Eqn. 1 as an example⁵ and synthesize LFP at a temperature of 1100 °C (2010 °F). A crushed piece of cast LFP ingot is shown in Figure 23. The LFP castings were evaluated and compared against the commercial LFP

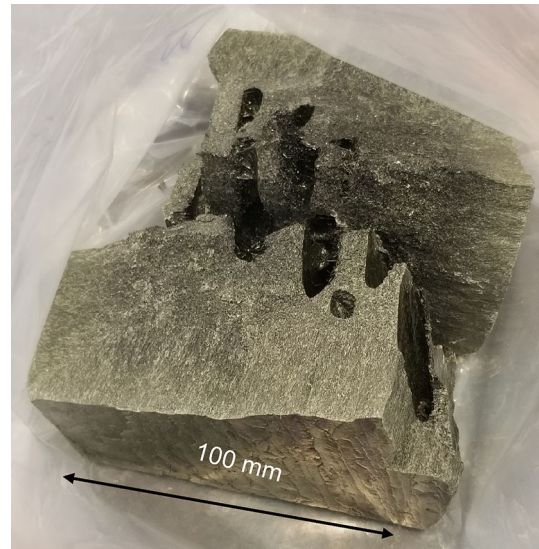
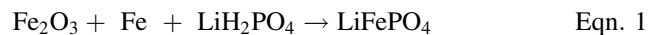


Figure 23. A crushed sample of LFP cast ingot.

product. Additional milling steps are required to reduce the cast LFP down to fine particles. Despite this drawback, the melt synthesis has various advantages to produce LFP with much lower cost. A measured cooling curve is shown in Figure 24. The T_L and T_S temperatures were determined as 1000 °C (1830 °F) and 880 °C (1615 °F), respectively, which agree with the DTA testing results presented in Figure 25. Compared to the TA cup method, the DTA testing led to a large undercooling of $\Delta T = 150$ °C. The DTA testing was conducted using a small sample of 0.2 g and under scavenging of argon gas flow, thus causing a largely undercooled LFP melt. For the TA cup and DTA methods, each one has its own advantages, e.g., foundry onsite testing for the former and two samples (to be tested and standard) controlled for the later.



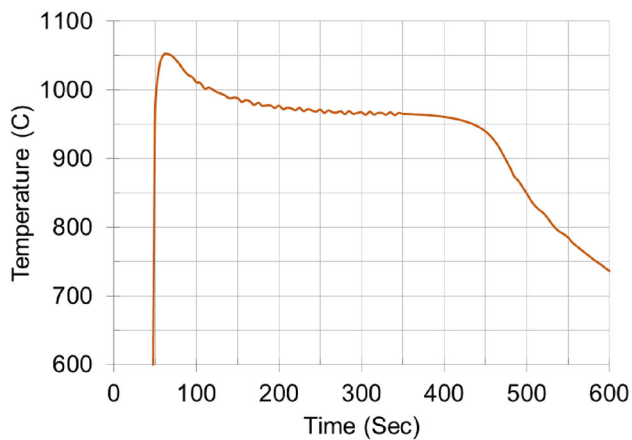


Figure 24. A measured cooling curve of LFP melt using the TA cup method.

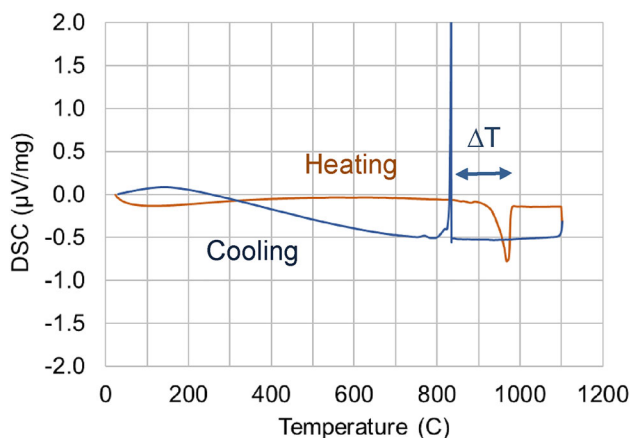


Figure 25. DTA curves of cast LFP sample showing $T_L = 980\text{ }^\circ\text{C}$ (1800 °F), $T_S = 880\text{ }^\circ\text{C}$ (1615 °F), and a large undercooling $\Delta T = 150\text{ }^\circ\text{C}$ in solidification.

Conclusions

Cooling curves were measured to assist the eight projects, namely high-Si cast iron (14.5% Si), high-Mn (18% Mn) steel, Al-alloyed stainless steel, high-entropy alloy AlCoCrFeNi_{2.1}, Permalloy 80 Ni alloy, Stellite Co alloy, EAF steelmaking slag, and lithium iron phosphate. The calculated phase diagrams show good agreement with the measured cooling curves. In addition, steelmaking slag foaming was studied, and lithium iron phosphate was synthesized using the induction melting method.

Acknowledgements

The work was performed at CanmetMATERIALS under the skillful contributions of P. Newcombe, H. Webster, D. Saleh, D. McFarlan, B. Ingram, B. Lacroix, G. Birsan, F. Benkel, J. Li, R. Zavadil, P. Liu, T. Smith, M. Aniolek, M. Podlesny, C. Shi, K. Sadayappan, A. Javaid, H. Jin, and C. DiGiovanni. The support of Canada OERD funding is gratefully

acknowledged. The projects were performed in collaboration with industrial companies (Wecast Industries ON, Elkem, Kennametal ON, Anotec BC, ArcelorMittal Dofasco, Stelco, and Ignis Lithium), universities (University of British Columbia, University of Alberta, McMaster University, University of Montreal, Polytechnique Montreal, and University of New Hampshire), and other Canmet laboratories (CanmetENERGY and CanmetMINING). Thanks are also due to the reviewers for the valuable comments and editing. This paper is based upon a presentation (2024-017) made at the 2024 AFS Metalcasting Congress and published in the AFS Transactions Vol. 132 (2024).

Funding

Open access funding provided by Natural Resources Canada library.

Open Access

This article is licensed under a Creative Commons Attribution 4.0 International License, which permits use, sharing, adaptation, distribution and reproduction in any medium or format, as long as you give appropriate credit to the original author(s) and the source, provide a link to the Creative Commons licence, and indicate if changes were made. The images or other third party material in this article are included in the article's Creative Commons licence, unless indicated otherwise in a credit line to the material. If material is not included in the article's Creative Commons licence and your intended use is not permitted by statutory regulation or exceeds the permitted use, you will need to obtain permission directly from the copyright holder. To view a copy of this licence, visit <http://creativecommons.org/licenses/by/4.0/>.

REFERENCES

1. H. Fredriksson, in ASM Handbook, Volume 15, Casting, ed. By D.M. Stefanescu, et al. (ASM International, 1998), p. 182.
2. D.M. Stefanescu, Thermal Analysis—Theory and applications in metalcasting. *Inter Metalcast* **9**, 7–22 (2015). <https://doi.org/10.1007/BF03355598>
3. R.B. Tuttle, In-depth analysis of steel cooling curves (23–066). *AFS Trans.* **131**, 403–412 (2023)
4. SFTA: solutionsfonderie.com/thermal-analysis/
5. M. Gauthier et al., Melt casting LiFePO₄ I. Synthesis and characterization. *J. Electrochem. Soc.* **157**, A453–A462 (2010)
6. P. Sauriol et al., Fe³⁺ reduction during melt-synthesis of LiFePO₄. *Canadian J. Chem. Eng.* **97**, 2196–2210 (2019)
7. Netzsch: DTA Testing Procedures Netzsch.
8. High-Silicon Iron Foundry: <https://anotec.com/>.

9. M. Blair et al., *Steel Castings Handbook* (ASM International, 1995), pp.1–21
10. K.G. Field, *et al.*, Handbook on the material properties of FeCrAl alloys for nuclear power production applications, U.S. DOE Report, M3FT-17OR020203031, 2017.
11. Y. Lu et al., A promising new class of high-temperature alloys: eutectic high entropy alloys. *Sci. Rep.* **4**, 1–5 (2014)
12. Permalloy 80: www.azom.com.
13. Stellite SF12: Kennametal.com/ca/en/.
14. C. DiGiovanni et al., Ranking of injection biochar for slag foaming applications in steelmaking. *Metals* **13**(1003), 1–14 (2023)
15. Website: The Canadian Critical Minerals Strategy.
16. L. Li, *Rare Earth Extraction and Separation* (Inner Mongolia S&T Press, 2011), pp.1–607
17. J.R. Davis, *ASM Specialty Handbook Cast Irons* (ASM International, 1999), pp.123–130
18. Foundry Handbook, Vol. 1, Cast Iron, in Chinese, 2nd edn. (China Machine Press, 2002), pp. 634-674.
19. D. Havel, Austenitic manganese steel, a complete overview, (Columbia Steel Casting Co., 2017) <https://www.scribd.com/document/394855437/2017-4-1-Columbia-Havel>
20. D.B. Miracle, O.N. Senkov, A critical review of high entropy alloys and related concepts. *Acta Mater.* **122**, 448–511 (2017)
21. D. Li, J. Li, Casting, forging and hot rolling of high-entropy alloy ingots (23–010). *AFS Trans.* **131**, 315–322 (2023)
22. A. Bogno et al., Amorphous phase formation analysis of rapidly solidified CoCr droplets. *Metall. Mater. Trans. B* **47**, 3257–3265 (2016)

Publisher's Note Springer Nature remains neutral with regard to jurisdictional claims in published maps and institutional affiliations.